IVYSPRING INTERNATIONAL PUBLISHER

Theranostics

2017; 7(6): 1735-1748. doi: 10.7150/thno.18352

Research Paper

Elongated Nanoparticle Aggregates in Cancer Cells for Mechanical Destruction with Low Frequency Rotating Magnetic Field

Yajing Shen[1*], Congyu Wu[1*], Taro Q. P. Uyeda[1, 2], Gustavo R. Plaza[1, 3✉], Bin Liu[4], Yu Han[5], Maciej S. Lesniak[5], and Yu Cheng[1✉]

1. The Institute for Translational Nanomedicine, Shanghai East Hospital, The Institute for Biomedical Engineering & Nano Science, Tongji University School of Medicine, Shanghai, 200120, China;
2. Department of Physics, Faculty of Science and Engineering, Waseda University, Tokyo 169-8555, Japan;
3. Center for Biomedical Technology, Universidad Politécnica de Madrid, 28223 Pozuelo de Alarcón, Spain;
4. Unit of Cell Death and Metabolism, Danish Cancer Society Research Center, Strandboulevarden 49, DK2100 Copenhagen, Denmark;
5. Northwestern University Feinberg School of Medicine, 676 North Saint Clair Street, Suite 2210, Chicago, Illinois 60611, United States.

* These authors contributed equally.

✉ Corresponding authors: gustavo.plaza@upm.es; yucheng@tongji.edu.cn

Received: 2016.11.15; Accepted: 2017.02.03; Published: 2017.04.10

Abstract

Magnetic nanoparticles (MNPs) functionalized with targeting moieties can recognize specific cell components and induce mechanical actuation under magnetic field. Their size is adequate for reaching tumors and targeting cancer cells. However, due to the nanometric size, the force generated by MNPs is smaller than the force required for largely disrupting key components of cells. Here, we show the magnetic assembly process of the nanoparticles inside the cells, to form elongated aggregates with the size required to produce elevated mechanical forces. We synthesized iron oxide nanoparticles doped with zinc, to obtain high magnetization, and functionalized with the epidermal growth factor (EGF) peptide for targeting cancer cells. Under a low frequency rotating magnetic field at 15 Hz and 40 mT, the internalized EGF-MNPs formed elongated aggregates and generated hundreds of pN to dramatically damage the plasma and lysosomal membranes. The physical disruption, including leakage of lysosomal hydrolases into the cytosol, led to programmed cell death and necrosis. Our work provides a novel strategy of designing magnetic nanomedicines for mechanical destruction of cancer cells.

Key words: Functionalized magnetic nanoparticles; Magneto-mechanical actuation; Brain cancer cells; Lysosome damage; Plasma membrane damage.

Introduction

Magnetic nanomaterials with remarkable magnetic properties and biocompatibility have been intensively investigated in the field of cancer treatment [1-4]. Magnetic nanoparticles (MNPs) are promising nanoplatforms for brain cancer therapy, owing to its capacity to cross blood–brain barrier (BBB) under the remote control of static magnetic field [5-10]. Previous studies have demonstrated that MNPs can be intravenously injected and guided by the external magnet to target brain tumors [7-9]. Fan et al. demonstrated that microbubbles loaded with doxorubicin-conjugated MNPs would target brain tumor under the static magnetic field, with enhanced drug delivery efficiency [10]. In addition to these applications, MNPs can be utilized as therapeutic agents for magnetic hyperthermia therapy employing an alternating magnetic field (AMF) [11-18]. MNPs can generate heat to increase the temperature and induce cancer cell death by an AMF at the high frequency of hundreds of kHz [12-15]. Currently, the magnetic hyperthermia therapy is under the clinical investigation for treating brain cancer patients and

has achieved moderate therapeutic outcomes [16,17]. The rapid heat generation can destroy the tumor microenvironment but could also be risky to damage the adjacent normal brain tissues [19].

The emergence of magneto-mechanical actuation has provided a potential and exciting strategy for cancer therapy [20-22]. Compared to heating, magnetic forces show the distinct advantages of localized actuation for the deeply seated tumors [23]. Thus, versatile magnetic nanomaterials have been developed in order to induce cancer cell death via mechanical stimuli, including multiwalled carbon nanotubes, permalloy, as well as iron oxide nanoparticles [24-26]. A recent study showed that iron oxide nanoparticles held the potential for magneto-mechanical destruction of cancer cells [27]. In order to improve the response of iron oxide nanoparticles to magnetic field, Zn, Ni and Co metal elements were doped into the nanoparticles to enhance the magnetization [28-30]. For instance, zinc-doped magnetic nanoparticles modified with the antibody of death receptor 4 can response well to the static magnetic field and mimic the TRAIL signaling pathway to induce the apoptosis of cells in zebrafish [31].

Epidermal growth factor receptor (EGFR), which is overexpressed in the majority of malignant brain tumors, is an important target for enhanced cancer therapy [32-34]. The EGFR-targeted nanoparticles can be efficiently internalized into the cells by receptor-mediated endocytosis and often accumulate in cell lysosomes [35]. Enhancing the permeability of lysosomal membrane is an effective strategy to promote cell death in the classic apoptotic pathways [36]. The EGF-modified iron oxide nanoparticles could destabilize the lysosomal membrane leading to a moderate cell death under the alternating magnetic field at 233 kHz [37, 38].

To establish an optimal strategy for brain cancer therapy, we report the novel application of combining high-magnetization zinc-doped iron oxide nanoparticles and a low frequency rotating magnetic field (RMF), at 15 Hz and 40 mT, to enhance the therapy by mechanical force. Compared to the micro-scale magnetic materials, nanomaterials are easily internalized by cells [39], and the intracellular cell membrane destruction has been proven to be more efficient than the disruption from the cell surface [23]. Furthermore, the magnetic field in this study is safe and its frequency substantially lower than the risk level in adults [40]. We reason that MNPs modified with the EGF peptide and internalized into lysosomes could assemble into elongated aggregates under the magnetic field and rotate when exposed to RMF, resulting in local mechanical damage of membranes and effective cell death. Here, we verified this hypothesis *in vitro* by utilizing the glioblastoma U87 cell line [41, 42]. Our results demonstrated that U87 cells were indeed efficiently damaged by the treatment.

Materials and Methods

Materials

Iron (III) acetylacetonate (97%), Dibenzyl ether (>98%) and Dopamine hydrochloride (DA) were purchased from Sigma. Zinc acetylacetonate hydrate (97%), morpholineethanesulfonic acid (MES), 1-(3-dimethylaminopropyl)-3-ethyl carbodiimide hydrochloride (EDC, > 98.0%), N-hydroxy succinimide (NHS, 98%) and N,N-Dimethyl-formamide (DMF) were purchased from Aladdin. Phosphate buffer saline (PBS), Dulbecco's Modified Eagle's medium (DMEM), penicillin/streptomycin and fetal bovine serum (FBS) were purchased from Hyclone. mPEG-NH_2 (MW=2000) was purchased from SINOPEG Biotech Co. Ltd (Xiamen China). Poly (acrylic acid) (PAA) (MW=2000) was purchased from Macklin Shanghai China. Epidermal Growth Factor (EGF) peptide was purchased from GL Biochem Ltd. (Shanghai). The CCK-8 kit and Propidium Iodide (PI) stain were purchased from Beijing Zoman Biotechnology Co., Ltd. Calcein, Fluo-4 AM and LDH cytotoxicity Assay Kit were purchased from Thermo Fisher Scientific, Shanghai, China. Ultra-pure water was used throughout all experiments. Matrigel was purchased from Corning, USA.

RMF equipment

The RMF station was assembled with two NdFeB magnets in a rotating cylinder (the device was fabricated by Niumag Co., Ltd., Shanghai, China). A motor was used to produce the magnets' rotation at 15 Hz and the cell-culture dish was placed above the station, at a distance of 5 mm, where the magnitude of the RMF was 40 mT.

Computation of the magnetic field

The magnetic field produced by the two permanent magnets in the spinning device was computed discretizing the magnets in 1000 cubes of homogeneous magnetization. The actual magnetization of the two magnets was calculated by fitting the measured value of the magnetic field along the rotation axis. The Figure 2 shows the magnetic field in two perpendicular planes.

Synthesis of Cube-shaped zinc doped magnetic nanoparticels and surface modification

The cubic magnetic nanoparticles with the average size of 62 nm were prepared by using a

previously published protocol [29]. Briefly, 52.61 mmol of benzyl ether and 3.78 mmol of oleic acid were added into a 50 mL three-neck, which was loaded with 0.8 mmol of iron (III) acetylacetonate and 1.2 mmol zinc(II) acetylacetonate. The mixture was exposed to the sonic machine for 30 min sonication, then it was heated to 290 °C for 30 min under an argon atmosphere and cooled to room temperature. Then 50 mL ethanol was added to the mixture to result in black precipitate. Finally, the product was centrifuged, isolated, and dispersed in toluene.

The procedure for preparation of DA-PAA-PEG modified magnetic nanoparticles (PEG-MNPs) was as reported by Li Z et al [43]. Briefly, PAA (0.01 mmol) and 0.125 mmol PEG-NH_2 were dissolved in 5 mL dimethylformamide (DMF), then 0.5 mmol (95.85 mg) 1-ethyl-3-(-3-dimethylaminopropyl) carbodiimide hydrochloride (EDC) and 104.5 μL triethylamine (TEA) were added to the mixed solution. The mixture was stirred for 24 h under the nitrogen atmosphere at room temperature. After adding 0.25 mmol DA, 0.25 mmol EDC and 70 μL TEA, the mixed solution at the same condition was stirred for another 24 h. The obtained suspension was purified by dialyzing against deionized water using dialysis membrane (MWCO 10,000) for 24 h. The solution was frozen dried to yield the final product DA-PAA-PEG and characterized via ^{1}HNMR.

Subsequently, to functionalize MNPs, 30 mg of the synthesized cubic magnetic nanoparticles were dispersed in 5 mL DMF. 40 mg of DA-PAA-PEG were dissolved in 10 mL deionized water and then mixed by sonication. The duration of the sonication was 50 min and the temperature was kept below 25 °C. After overnight reaction, the excess DA-PAA-PEG was removed by magnetic separation. The product was washed with water and redispersed in deionized water.

Conjugation of EGF peptide the surface of MNPs

Briefly, 20 mg of PEG modified MNPs were dissolved into 4 mL MES solution (pH=4.8). Then 0.5 mmol of EDC and 0.6 mmol of NHS were added. Herein, EDC was applied to activate the terminal carboxyl groups on the PAA chains of PEG modified magnetic nanoparticles (PEG-MNPs) for conjugation with primary amines of EGF peptide. NHS was used to improve the efficiency of EDC-mediated coupling reactions by stabilization of the amine-reactive intermediate. The reactant was shaken at room temperature for 15 min. Then, 4.8 mL of basic phosphate buffered saline (PBS) were added with stirring. 80 μL of EGF peptide (10 μg/μL) were added immediately. The resultant suspension was shaken at room temperature during 24 h. Free EGF peptide was removed by magnetic separation. Bicinchoninic acid (BCA) protein assay was used to quantify the peptide conjugation on the MNPs. In addition, FITC labeled EGF peptide was conjugated with the MNP to confirm the surface modification.

Construction of PEG-MNPs/FITC and EGF-MNPs/FITC

Briefly, 4 mg of the PEG-MNPs or EGF-MNPs were dispersed in 3 mL of deionized water. Then 1mL of 0.01 mg/mL fluorescein isothiocyanate (FITC) ethanol solution was added. After ultrasonication for 30 min, the solution was mixed overnight. Finally, the PEG-MNPs/FITC or EGF-MNPs/FITC were collected by magnetic separation and washed with ethanol three times to remove the excess FITC.

Morphology and structure characterization

The morphology and average size of MNPs and EGF-MNPs were characterized by using transmission electron microscopy (TEM, JEM-1230, JEOL Ltd.) without staining. The hydrodynamic size and Zeta potential of EGF-MNPs were measured in deionized water with a concentration of 10 μg/mL, using a particle size analyzer (Zeta SIZER NANO ZS90, Malvern Ltd.). The crystalline phase of the MNPs were characterized by means of X-ray diffraction (XRD) measurements using Cu Kα radiation (λ = 1.54 Å) on a diffractometer (Y-4Q, China) in 2θ range of 10^o ~ 70^o. The static magnetic properties of dry MNPs at room-temperature were measured with Vibrating Sample Magnetometer (VSM, Lakeshore 7407, US).

Cell culture

Glioblastoma U87 cells (American Type Culture Collection, Manassas, VA., USA) were cultured and maintained in DMEM supplemented with 10% fetal bovine serum (FBS) and 100 U/mL penicillin, 100 μg/mL streptomycin and incubated at 37 °C under a humidified atmosphere containing 5% CO_2.

In vitro cytotoxicity study

The cytotoxicity of EGF-MNPs in U87 cells was evaluated using a MTT assay. Before incubation, PEG-MNPs and EGF-MNPs were sterilized for 24 h with UV-light, then diluted in DMEM medium and mixed thoroughly. Then 1 × 10^4 cells were seeded into 96-well plates and incubated at 37 °C overnight. Subsequently, the culture medium in each well was replaced with fresh medium that contained PEG-MNPs or EGF-MNPs in a series of concentrations. Cells in wells without the addition of MNPs were used as a control group. Each group included five replicates. After culturing for further 24 h, 10 μL of MTT solution were added and cell viability

was calculated as the ratio of the absorbance of test and control wells. The absorbance was measured at 570 nm by using a microtiter plate reader (ELx808, BioTek).

TEM Observation for Cellular Uptake of MNPs

U87 cells were seeded in Φ 60 mm dishes with the density of 2 × 10^5 cells per dish. After overnight incubation, the culture media was replaced by 100 μg/mL PEG-MNPs and EGF-MNPs, and incubated for 24 h. For TEM studies, excess medium of each dish was removed and the dish was washed with PBS buffer three times. The cells were trypsinized and harvested through centrifugation at 1000 rpm for 5 min. Then, the cell pellets were fixed with 2.5% glutaraldehyde overnight at 4 °C. Subsequently, they were fixed with 1% aqueous osmium tetroxide and dehydrated using acetone in a series of concentrations and embedded in Epon Araldite resin. Ultrathin sections of 100 nm containing the cells were placed on the grids and double contrasted with 4% uranyl acetate (1:1, acetone:water) and 0.2% Reynolds lead citrate (water). Finally, the samples were air-dried. TEM images were obtained under 300 kV in a FEI Tecnai F30 microscope equipped with a Gatan CCD digital camera.

ICP-OES

Inductively coupled plasma-optical emission spectroscopy (ICP-OES) was performed to quantify the MNPs that were taken up by cells. Cells were seeded in 12-well plates with the density of 1.2 × 10^5 cells per well, and incubated with 100 μg/mL of PEG-MNPs and EGF-MNPs for 1, 4, and 24 h, respectively. After incubation, cells were washed three times with PBS and then trypsinized and collected. Cells were counted in a blood cell counting chamber. The cell pellet was collected by centrifugation and lysed with nitric acid. The content of Fe was measured by ICP-OES (Thermo iCAP 7600 ICP-OES).

Quantification of U87 cell death by the treatment with EGF-MNPs and low frequency RMF

To investigate the destructiveness of EGF-MNPs to cells under low frequency RMF, cell viability tests were performed. 96-well plates were seeded with cells with the density of 1 × 10^4 cells per well. Then six of the plates were incubated with 100 μg/mL EGF-MNPs and the other three plates were used as control samples. After 24 h of incubation, the cells were exposed to RMF treatment for three days (30 min every day). CCK-8 assay was used to analyze the cells viability day by day. The absorbance was measured at 450 nm by using a microtiter plate reader.

Confocal Microscopy

U87 cells were seeded on confocal laser dishes with the size of Φ35 mm at the density of 5 × 10^4 cells per dish and stabilized for 24 h. 100 μg/mL of EGF-MNPs labelled with FITC in culture medium were added to the dish and the cells were incubated for 24 h. After being washed with PBS three times, Lysosome tracker Red (5 ×10^{-7} mol/L) was used for lysosome and stained for 45 min. Then the cells were washed three times with PBS, and fluorescent images were taken by confocal microscopy (Leica TCS SP5). The quantification of the co-localization with lysotracker red for PEG-MNPs or EGF-MNPs were analyzed through Image-Pro Plus software.

Study of the cell death under RMF

U87 cells were seeded on confocal dishes and cultured for 24 h. Then the cells were treated with 100 μg/mL EGF-MNPs in 1 mL culture medium. After 24 h incubation, the cells were washed three times with PBS to remove the extra nanoparticles. The RMF was applied at 15 Hz for 10 min. The two control groups were as follows: one dish without EGF-MNPs, the other one incubated with the same concentration of EGF-MNPs but without RMF treatment. Then the live/death cells were examined by using the Calcein AM/PI staining kit. The results in U87 cells were monitored under a Live Cell Imaging System (EVOS FL Auto, Life Technologies).

Assessment of liposomal membrane permeabilization

According to the previous work by Aits et al. [44], the plasmid pCDH-EF1-EGFP-LGALS3, abbreviated as EGFP-Gal3, was created by cloning human LGALS3 (isoform 1) sequences into lentiviral pCDH-EF1-MCS-IRES-Neo vector (Systems Biosciences, CD533A-2) which possessed N-terminal EGFP tags. U87 cells were placed on confocal dishes 24 h before experiments. By utilizing Lipofectamine 2000, these cells were transiently transfected by the plasmid 24 hours until the LGALS3-GFP were expressed. Afterwards, the cells were incubated with 100 μg/mL EGF-MNPs for 24 hours, then the cells were kept under RMF for another 30 min. Subsequently, the images of these cells were captured using the Live Cell Imaging System just after treatment. The amount of the puncta was analyzed, taking into account that it varies linearly with that of the permeable lysosomes.

Physical destruction of cell membrane

U87 cells were grown on confocal dishes until

they adhered. The cells were incubated with 100 μg/mL EGF-MNPs which dispersed in 1 ml culture medium. Twenty-four hours later, unbinding EGF-MNPs were removed and the culture medium with 10 μg/mL of propidium iodide (PI) was added. Exposing subsequently the sample to RMF for 10 min, the cells in dishes were placed immediately in the Live Cell Imaging System. In this experiment we limited the RMF treatment to 10 minutes to avoid PI-cytotoxicity effects over longer times.

Flow cytometry analysis

The cells were seeded in confocal dishes at the density of 1×10^5 cells per dish and then incubated with the EGF-MNPs (100 μg/mL) for 24 h. After being washed three times with PBS to remove the free EGF-MNPs, the cells were treated with RMF for 30 min. After incubation for additional 24 h, the cells were collected and washed with PBS for three times. Then the cells were stained with 5 μL Annexin V-FITC and 10 μL PI for 15 min at room temperature in dark. The cells were analyzed with a flow cytometer (AttuneNxT flow cytometer, Life Technologies, Thermo Fisher, USA)). The data were examined using the FlowJo software (FlowJo Llc, Ashland, Oregon, USA). Cells incubated with the growth medium and EGF-MNPs without RMF treatment were used as control groups, respectively.

Statistical analysis

All statistical analyses were performed using Graphpad Prism 5 (GraphPad Software Inc., San Diego CA). The sample number for each group was ≥3 and numerical data were reported as Mean ± SD. p values were considered to be statistically significant at $^*p<0.05$, $^{**}p<0.01$, $^{***}p<0.001$.

Results and Discussion

Synthesis and Characterization of EGF-MNPs

The synthesis of EGF peptide modified PEG-MNPs (EGF-MNPs) is illustrated in Figure 1a. The cubic MNPs were synthesized via thermal decomposition in benzyl ether and modified with DA-PAA-PEG to achieve solubility in aqueous solutions [29, 43]. The DA-PAA-PEG modified magnetic nanoparticles (PEG-MNPs) were further conjugated with EGF peptide (YHWYGYTPQNVI-amide) to obtain the EGF-MNPs. The transmission electron microscopy (TEM) images showed that the MNPs had the cubic shape (Figure 1bi) with the average length of 62.1 ± 0.8 nm (Supplementary Figure S1b). Compared to MNPs, the PEG-MNPs and EGF-MNPs had an obvious polymer shell on the surface of MNPs as shown in TEM images (Figure 1b). Based on DLS, the hydrodynamic diameters of PEG-MNPs and EGF-MNP were 190 nm and 220 nm (Supplementary Information, Figure S1d), respectively. Energy-dispersive X-ray spectroscopy (EDS) analysis (Figure S1a) confirmed the content of Zn and Fe with stoichiometry $Zn_{0.4}Fe_{2.6}O_4$ in the MNPs, which was in agreement with previous results [45]. In addition, X-ray diffraction (XRD) patterns of MNPs matched well with the bulk Fe_3O_4 (JCPDS #: 19-0629) revealing their spinel crystal structure (Figure 1c) [29]. Remarkably, the saturation magnetization of MNPs and EGF-MNPs were 78 and 68 emu g^{-1}, respectively, as shown in Figure 1d. The magnetization vs. magnetic field curves showed a very low coercivity (105 Oe), thus the products behaved similarly as superparamagnetic nanoparticles. With the Zn^{2+} doping, the obtained MNPs had better magnetization properties than typical ferrite-based nanoparticles, which could improve the magneto-mechanical actuation for further studies [46].

PEG-MNPs had the Zeta-potential of -7.37 mV due to the carboxyl groups of DA-PAA-PEG on the surface (Figure S1c). After peptide conjugation, EGF-MNPs showed slight positive surface charge with Zeta-potential of +6.93 mV (Figure S1c). In addition, to confirm the peptide conjugation, FITC labeled EGF peptide was used to modify the MNPs. Fluorescence spectra (Figure S1e) of free FITC-EGF peptide and FITC-EGF-MNPs showed a similar emission peak centered at 517 nm, which corresponded to the characteristic fluorescence emission band of FITC. Furthermore, BCA assay was used to provide the numeric information regarding peptides on MNPs surface (Figure S1f). The content of EGF peptide in the modified MNPs was 0.123 mg/mL, suggesting the successful peptide conjugation on the surface of MNPs.

RMF and its effect on the MNPs

The RMF device was assembled via permanent magnets to produce a RMF (40 mT), with the aim of generating mechanical forces that could damage cancer cells at low frequency. A scheme of this device is shown in Figure 2a and 2b. The magnetic field produced by the device is shown in Figure 2c. It has been reported that MNPs may align and assemble by the effect of magnetic fields [47,48]. As shown in Figure S7, the EGF-MNPs could form the aggregates with elongated shapes only under the magnetic field. These aggregates were magnetically anisotropic with easier magnetization along the longitudinal direction (i.e. the direction of larger size). The torque $\vec{\tau}$ on an aggregate could be calculated by $\vec{\tau} = \vec{m} \times \vec{B}$, where $\vec{m}$ is the total magnetic moment of the aggregate and $\vec{B}$ is the external magnetic field [49]. An estimate of the

maximum value of the torque may be obtained by assuming the magnetization of the aggregate is negligible in the transversal direction compared to the longitudinal direction.

In the experiment shown in Figure 2d, EGF-MNPs were embedded in the matrigel matrix to provide viscosity and mimic the biological environment inside the cells. Under the RMF, the elongated aggregates were formed with the size of ~4 μm in the longitudinal direction and could rotate with the magnetic field (Figure 2e). The large aggregates contained ~10^3 MNPs in the two-dimensional image and could generate sufficient force to overcome the friction forces. The magnetic torque $\vec{\tau}$ is proportional to the number of MNPs in the aggregate. For a reference number of 10^3 nanoparticles (of cubic shape with thickness of 60 nm), it would be in the order of 4×10^2 pNμm and the maximum related forces would be in the order of hundreds of pN (see Supplementary Material and scheme in Figure 2d and 2e), nearly reaching the lower limit of forces required to disrupt the cell membrane, of hundreds of pN [50]. It should also be noted that the viscosity could play a role to control the movement of the aggregates. The upper aggregate could move easily compared to the bottom one (Figure 2d), which could be due to the different viscosity caused by inhomogeneity of the matrigel. In the case of synchronous rotation, the magnetic torque must be balanced by the friction forces (as shown in Figure 2e) to produce a constant rotation frequency. The phase difference between magnetic field and the aggregate is required to reach this balance. If the viscosity is higher the aggregates may still rotate non-synchronously. When the viscosity and friction forces in the surrounding medium are sufficiently low, the aggregates of nanoparticles can rotate synchronously with the magnetic field, as illustrated in Figure 2d.

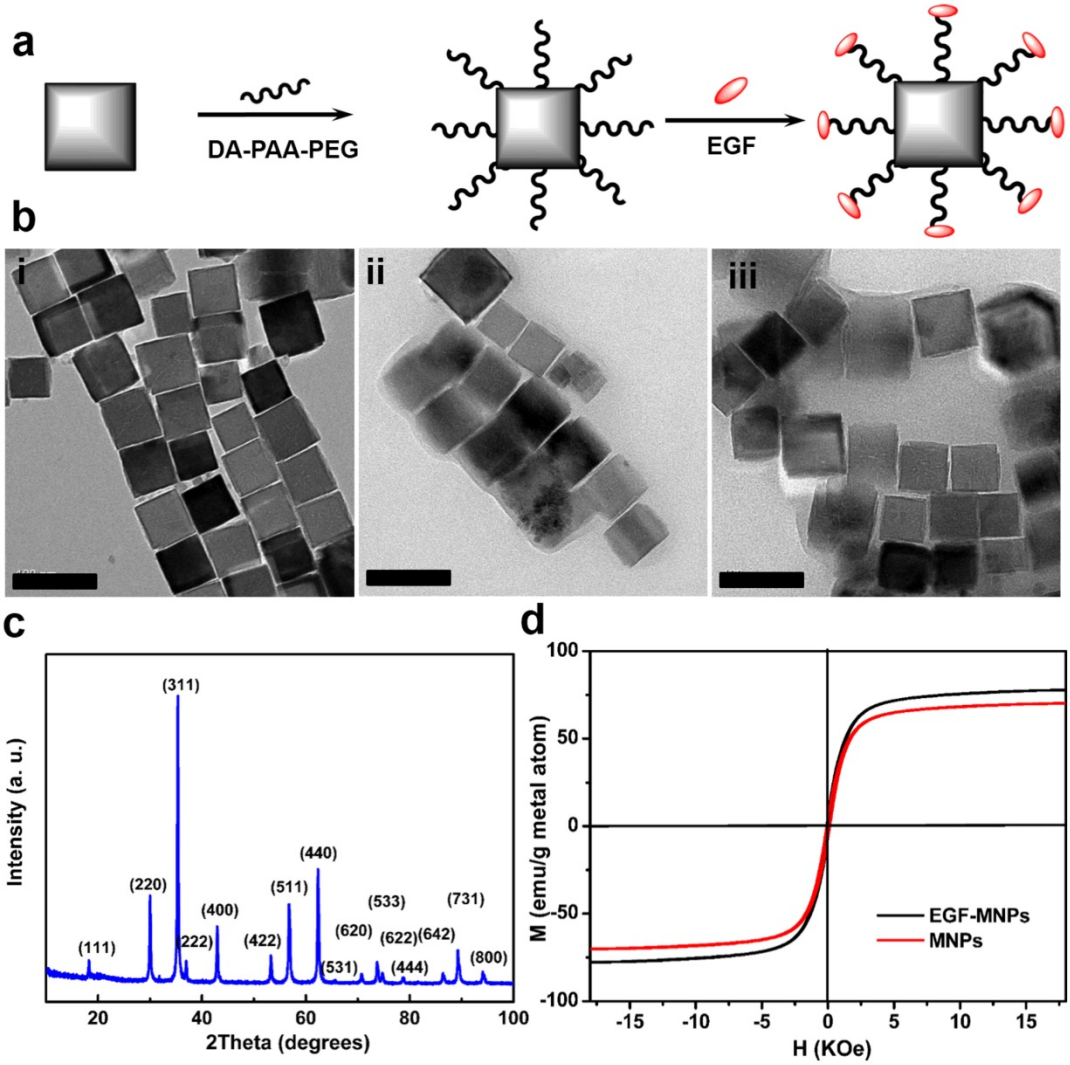

Figure 1. Characterization of MNPs and EGF-MNPs. (a) Scheme of the synthesis of EGF-functionalized MNPs. (b) Representative TEM images of (i) MNPs, (ii) PEG-MNPs and (iii) EGF-MNPs. (c) X ray diffraction pattern of MNPs. (d) Magnetization vs. magnetic field curves of dry MNPs and EGF-MNPs at 300 K. The size of scale bars is 100 nm.

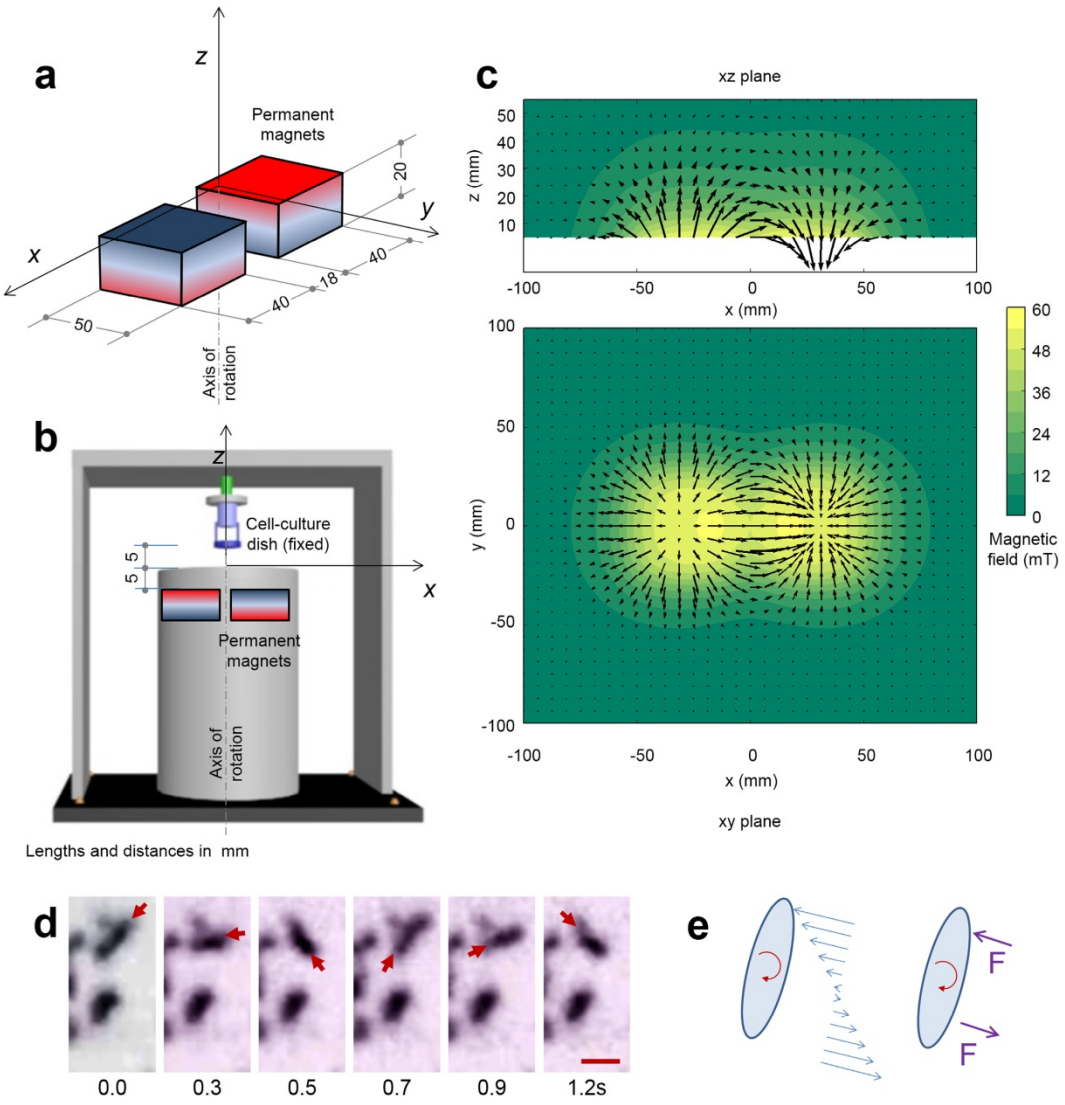

Figure 2. RMF and its effect on the MNPs. (a) Dimensions of the two NdFeB permanent magnets used in the equipment and reference axis. (b) Position of the two magnets in a rotating cylinder in the device and location of the cell-culture dish. (c) Representation of the magnetic field in the axial plane xz and in the transversal plane xy, both containing the center of the cell-culture dish; the modulus of the field is displayed in color scale and arrows represent its projection to the planes. (d) Aggregates of magnetic nanoparticles in a matrigel (concentration of 1 mg/mL) during the rotation of the magnetic field at 0.67 Hz. The series of images shows one aggregate rotating synchronously with the magnetic field (upper, the arrow indicates the position of one end) and one aggregate which does not rotate. The size of the scale bar is 5 μm. (e) Scheme of the friction forces per unit length acting on a rotating aggregate of nanoparticles and the equivalent point forces; during the synchronous rotation the magnetic torque is balanced by the friction forces.

Intracellular uptake of EGF-MNPs

Next, the uptake of EGF-MNPs and targeting ability was investigated on the brain cancer cells. The hypothesis was that, based on the interaction between EGF peptide and EGFR overexpressed on tumor cell membrane, EGF-MNPs would be rapidly internalized by U87 cells and subsequently accumulated into lysosomes [51]. The cytotoxicity of EGF-MNPs was investigated (Figure S2). The EGF-MNPs were non-toxic up to 200 μg/mL after 24 h incubation. Figure 3 showed that the EGF-MNPs accumulated in cells and were localized in lysosomes after 24 h internalization (Figure 3a). ICP-OES analysis indicated that the cells treated with EGF-MNPs had an overall 2-3 fold increase of intracellular Fe content compared to those incubated with PEG-MNPs at different incubation time points (Figure S3), indicating the selective uptake of EGF-MNPs into glioma cells. Moreover, the subcellular location of PEG-MNPs and EGF-MNPs labeled with FITC was studied by utilizing laser scanning confocal microscope (CLSM). The U87 cells were stained with LysoTracker Red to visualize lysosomes after incubation with EGF-MNPs-FITC. As expected, the majority of EGF-MNPs-FITC colocalized with the LysoTracker Red probe, as shown in Figure 3b. In contrast, sparse PEG-MNPs distributed in lysosomes were observed by TEM and CLSM (Figure 3a and Figure S9b). These results both proved that a large number of EGF-MNPs were efficiently internalized by U87 cells and trapped in lysosomes.

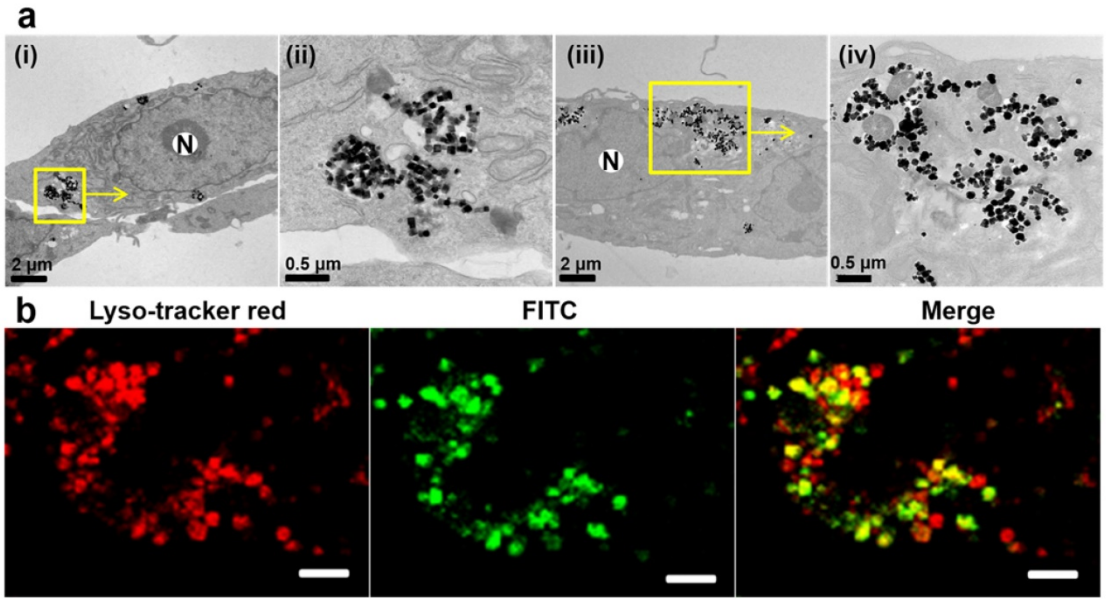

Figure 3. Representative images of the internalized MNPs. (a) TEM images of U87 cells incubated with 50 μg/mL of PEG-MNPs (i), (ii) and EGF-MNPs (iii), (iv) for 24 h; (ii) and (iv) show enlarged views of the rounded areas. N represents the nucleus. (b) Confocal images of U87 cells incubated with 100 μg/mL of EGF-MNPs during 24 h at 37 °C. Cell lysosomes were stained by lysosome tracker red and the magnetic nanoparticles were labeled by FITC. The images (from left to right) were taken immediately after lysosome tracker red staining for 30 min, at excitations of 488 and 577 nm, respectively. Yellow spots show the lysosome co-localization coming from the merged green and red signals. The size of the scale bars is 10 μm.

Lysosomal membrane rupture

Lysosomes are crucial organelles that participate in many cellular processes related to cell homoeostasis [44]. Saftig P et al. have reported that lysosomal membrane permeabilization (LMP) can induce the leakage of lysosomal hydrolases into the cytosol, and lead to cell death eventually [52,53]. Accordingly, based on the effect of a RMF on aggregates of EGF-MNPs, described above, we hypothesized it would be possible to induce cell death through destruction of lysosomal membrane that contain large aggregates of EGF-MNPs. Here, for the sensitive detection of LMP, the galectin-based strategy was utilized to investigate LMP. Galectins are soluble carbohydrate-binding lectins which exist in the cytosol, nucleus and extracellular environment [54]. When LMP occurs, galectins are recruited to the site of lysosomal damage and form puncta. Thus, the U87 cells were transfected with a plasmid that expresses EGFP-Galectin3 (Gal3) and evaluated formation of galectin puncta (detected as fluorescent dots) that served as markers for LMP [44]. Before RMF treatment, both control cells (without MNPs) and cells incubated with EGF-MNPs exhibited just diffuse green fluorescence in the cytoplasm. In contrast, several distinct fluorescent puncta appeared in cells after the RMF treatment at 15 Hz for 30 min (Figure 4a), indicating the occurrence of damage of the lysosomal membranes [55]. Two factors were considered to choose this low rotation frequency to test our nanoparticle system. Firstly, the magnetic field in the order of tens of Hz could generate mechanical force without generation of heat [27]. Secondly, the fabrication of the rotating device is simple with reasonably low cost by assembly of permanent magnets. Therefore, this approach could be easily adapted for magneto-mechanical actuation.

Occurrence of lysosomes rupture was confirmed by TEM images. U87 cells incubated with 100 μg/mL of EGF-MNPs for 24 h had lysosomes loaded with EGF-MNPs and with irregular shape (Figure S5 MF-), surrounded by the lysosomal membrane composed of a single 7–10 nm thick phospholipid bilayer (red arrows) [56]. As shown in Figure 4b, after the treatment with the RMF, EGF-MNPs assembled into elongated aggregates of micrometer size and escaped from the lysosomal membranes (Figure 4bi and 4bii). The integrity of lysosomal membrane was disrupted (yellow arrows in Figure 4bii) and the EGF-MNPs escaped into the cytoplasm as shown in Figure 4bii (red arrows). Importantly, the EGF-MNPs could also partially destroy the plasma membrane and be excreted into the surrounding environment (Figure 4iv). The morphology of the treated U87 cells was changed (Figure S4a) and in some cases the cell membrane was destroyed dramatically (Figure S4b).

Based on the TEM images, the size of the elongated aggregates in lysosomes was in the range of 0.5 to 5 μm in the two dimensional slide section with the thickness of 100 nm. It is estimated that the aggregates containing 10^3–10^4 EGF-MNPs could generate the torque in the order of 4×10^2 pNμm. Therefore, hundreds of pN force could be reached

under RMF. The movement of the aggregates in the cells was confirmed by live cell imaging (Video S1). It has been reported previously that a torque of 10-30 pNμm and forces of 20-50 pN using micrometer-size discs and an alternating magnetic field (20 Hz, 0.01 T) produced loss of human-glioma-N10 cell membrane integrity [25]. The thickness of those discs was nearly 60 nm and therefore their volume was smaller than the biggest aggregates in the present work. Therefore, it is likely that the big aggregates of our system, with 10^3–10^4 nanoparticles, could produce the forces required to rupture membranes. The big size of the aggregates, thus, allows producing relatively large forces compared to the conventional nanoparticle systems.

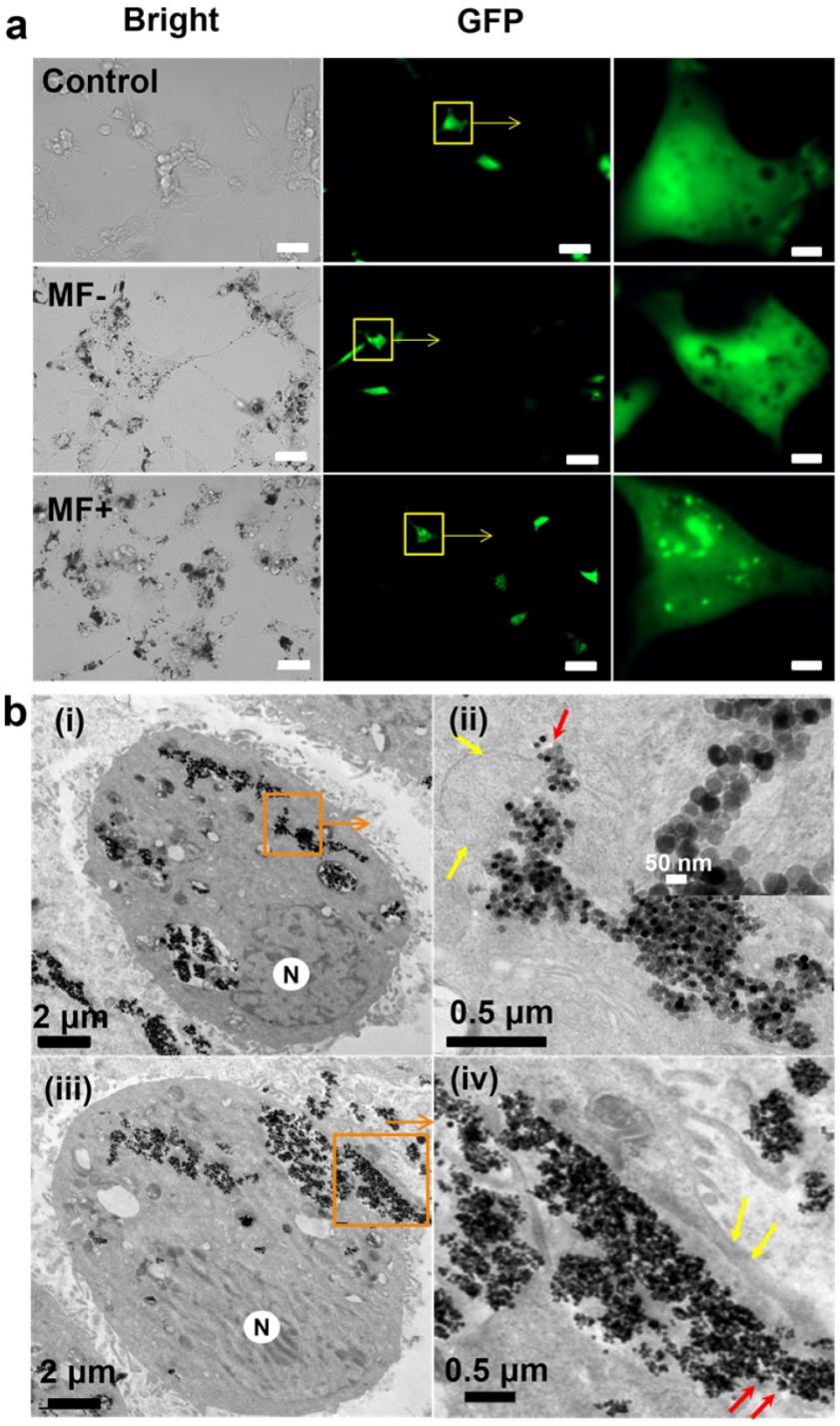

Figure 4. Effect of the treatment with EGF-MNPs under RMF. (a) Fluorescence images of U87 cells transfected with EGFP-Gal3 plasmid, then incubated with 100 ug/mL EGF-MNPs for 24 h before the RMF treatment (15 Hz, 30 min). The size of the scale bars is 50 μm in the bright-field and fluorescence images, and 5 μm in the enlarged areas of the fluorescence images. (b) TEM images of U87 cells which incubated with 100 μg/mL of EGF-MNPs for 24 h, then exposed to RMF treatment for 30 min. (i shows lysosomal membrane destruction and iii shows cell membrane destruction. ii and iv are the enlarged view of the boxed areas. The inset is the boxed area in ii shows the aggregates of EGF-MNPs in lysosome. The lysosome and cell membrane are indicated by yellow arrows. "N" represents the nucleus.)

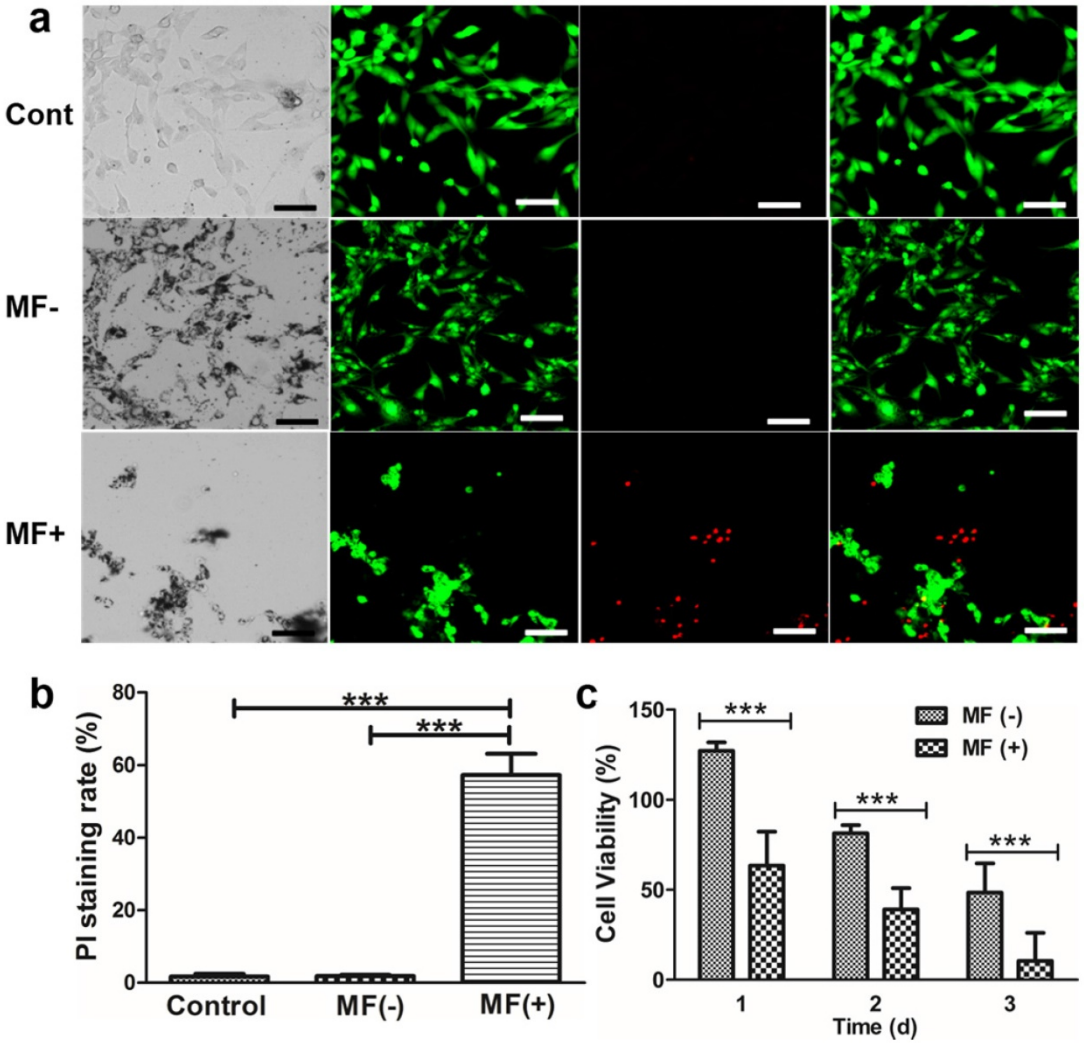

Figure 5. Live-cell imaging of U87 cells. (a) Fluorescence micrographs of control cells without EGF-MNPs but applying the RMF treatment (upper), cells incubated with EGF-MNPs but without applying RMF treatment (MF-, middle) and cells incubated with EGF-MNPs and treated with RMF treatment (MF+, bottom). The concentration of EGF-MNP was 100 μg/mL and the incubation time was 24 h. RMF treatment was at 15 Hz for 10 min. Live/dead cells were green/red (Calcein AM/PI), respectively. All scale bars are 50 μm. (b) The PI staining ratios of control, MF- and MF+ cells. Six different areas were analyzed. (c) Viability of U87 cells incubated with 100 μg/mL EGF-MNPs for three days, assayed by CCK8 assay. One group without RMF as the control and the other was treated with RMF for 30 min every day. *** shows that the pair is statistically different ($p<0.001$).

Physical destruction of cell membrane

As described in the previous paragraphs, the combined effect of EGF-MNPs and RMF could affect the lysosomal membrane integrity, the cell morphology and the cell membrane. Thus, to further evaluate the damage to the cell membrane by the RMF treatment, we assayed permeability of cell membrane using two fluorescence indicators, i.e., calcein AM and propidium iodide (PI). Calcein AM is a cell permeable, green fluorescent dye. After cleavage by a ubiquitous intracellular esterase, however, it is retained inside live cells unless the cell membrane becomes damaged and permeable. In contrast, PI, a DNA-binding red fluorescent dye, is cell membrane-impermeable and only stains nuclei of cells without intact cell membrane. Initially, the U87 cells were incubated with 50 μg/mL and 100 μg/mL EGF-MNPs, respectively (Supplementary Information, Figure S6). As shown by PI staining, EGF-MNPs did not produce cell membrane destruction. After being exposed to the RMF treatment, many cells were stained with PI, increasing with the concentration of EGF-MNPs (Supplementary Information, Figure S6). As shown in Figure 5a, most cells treated with RMF were stained with PI, while no cells showed red fluorescence in control and MF- groups. Next, for quantitative analysis, calcein AM and PI were used to distinguish live and dead cells. First, average fraction of cells with permeabilized plasma membrane, defined as the proportion of PI positive cells in total cells, was calculated (Figure 5b). The fraction of cells affected by the EGF-MNPs under RMF was 57.4% ± 5.8%, while control of non-treated cells was 1.7% ± 0.7% and cells incubated with particles in the absence of RMF was 1.8% ± 0.3%. It

was demonstrated that cell membrane could be efficiently disrupted by RMF after incubation with EGF-MNPs. Nonetheless, accumulation of EGF-MNPs did not cause higher cytotoxicity, since the MTT assay found that cell viability decreased only slightly after exposure to up to 200 μg/mL EGF-MNPs for 24 h (Figure S2). Furthermore, the result of the MTT assay (Figure 5c) was consistent with the results of Calcein AM/PI staining (Figure 5a). Because of the oxidative stress induced by long-time incubation with EGF-MNPs, the viability of the cells (without RMF treatment) reduced progressively (Figure 5c) [57,58]. This result showed that the EGF-MNPs possessed low acute cytotoxicity being suitable for cancer therapy.

It has been proved that LMP can induce cell death via apoptosis [59]. After the RMF treatment, Annexin V, a protein with high affinity for phosphatidylserine, was found to stain the cells (Figure 5c). It showed that the EGF-MNPs could cause the programmed cell death under the RMF treatment. To more directly evaluate cell death induced by our system of EGF-MNPs *in vitro*, the cellular viability was studied via CCK-8 assay following RMF treatment. After incubation with 100 μg/mL EGF-MNPs for 24 h, the cells were treated with RMF for 3 days (30 min per day). During three-day treatment, the cell viability declined gradually (Figure 5c), being significantly lower than in cells without RMF treatment. Over 90% of the cells were damaged post the treatment.

Apoptosis determined by Annexin V-FITC/PI staining

Cells were incubated with EGF-MNPs (100 μg/mL) and exposed to RMF for 30 min. Cell death was studied by Anexin V-FITC/PI staining and quantified by flow cytometry (Figure 6). Apoptotic cells were observed in fluorescence micrographs in the RMF treated group (Figure 6a, green fluorescence by AnnexinV-FITC). Compared to the non RMF treated group, EGF-MNPs induced programmed cell death under RMF, indicating the physical force could also actuate the internal biological behaviors. The quantitative results of the flow cytometery were also shown in Figure 6b. After the RMF treatment, 3.8% of cells underwent early apoptosis and 16.9% were late apoptotic cells. The apoptotic ratio of MF- group was similar to the control (no MNPs, no treatment) group. The flow cytometry data demonstrated that the RMF treatment could induce apoptosis by increasing the permeability of lysosomes.

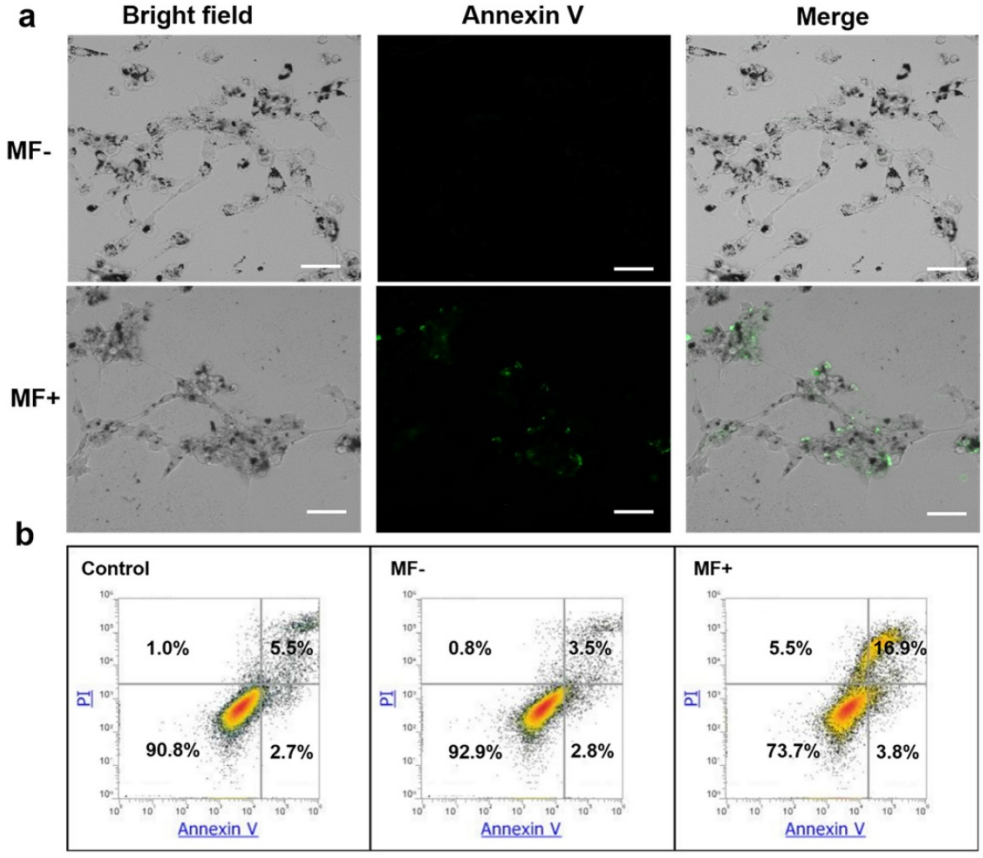

Figure 6. Cell death mechanism induced by RMF treatment in U87 cells. (a) Fluorescence micrographs of cells incubated with EGF-MNPs for 24 h. With (MF+) and without (MF-) RMF treatment, the cells were stained with Annexin V-FITC. All scale bars are 50 μm. (b) Flow cytometry analysis of U87 cells after incubation with 100 μg/mL EGF-MNPs for 24 h, again with/without RMF treatment. Cells were cultured and stained with Annexin V-FITC/PI before analyzed by flow cytometry.

The proposed cell-death mechanism is summarized in Figure 7. EGF-MNPs can selectively enter cancer cells through intracellular endocytic pathways and rapidly concentrate in the lysosomes of the cells. When exposed to the low frequency RMF, EGF-MNPs form elongated aggregates along the field direction that can produce a torque. It has been revealed that, when low frequency RMF was applied, the EGF-MNPs assembled into elongated shapes with magnetic anisotropy property. After consistent interaction with the membranes via mechanical force during RMF, they efficiently damaged lysosomes and plasma membrane, inducing apoptotic and necrotic cell death. Additionally to the damage of membranes, mechanical forces could stimulate signaling pathways through the gating of mechanotranduction channels on the cell membrane. In particular, it could be a future study of the activation of the calcium ion channel in this system, since it is one of the most important components for triggering apoptosis and it could be manipulated by the mechanical forces [25].

Recent works have shown that magneto-mechanical actuation within cells could be exploited for tumor treatment [21-27]. Although previous studies have demonstrated that magnetic nanoparticles can induce cell death via mechanical force, their efficacy is still limited. Part of the reason is the inefficient response of nanoparticles to the applied field. As a result, we designed zinc-doped MNPs to enhance the intrinsic magnetic properties and applied the magnetic field to assemble the MNPs inside of the cells, which could produce hundreds of pN force comparable to the microscaled particle systems. Furthermore, in order to improve the targeting ability of the MNPs, EGF peptide was conjugated on the MNPs for selective targeting the U87 cells with over expression of EGFR on the cell membranes and promoting the accumulation in lysosomes via endocytosis [35]. Consequently, the magnetically anisotropic aggregates in the lysosomes could effectively rotate and break the lysosomes and cell membranes under RMF. Taken together, the magneto-mechanical actuation via these elongated aggregates in the cells could effectively destroy the cancer cells synergistically by both of the physical and biological effects.

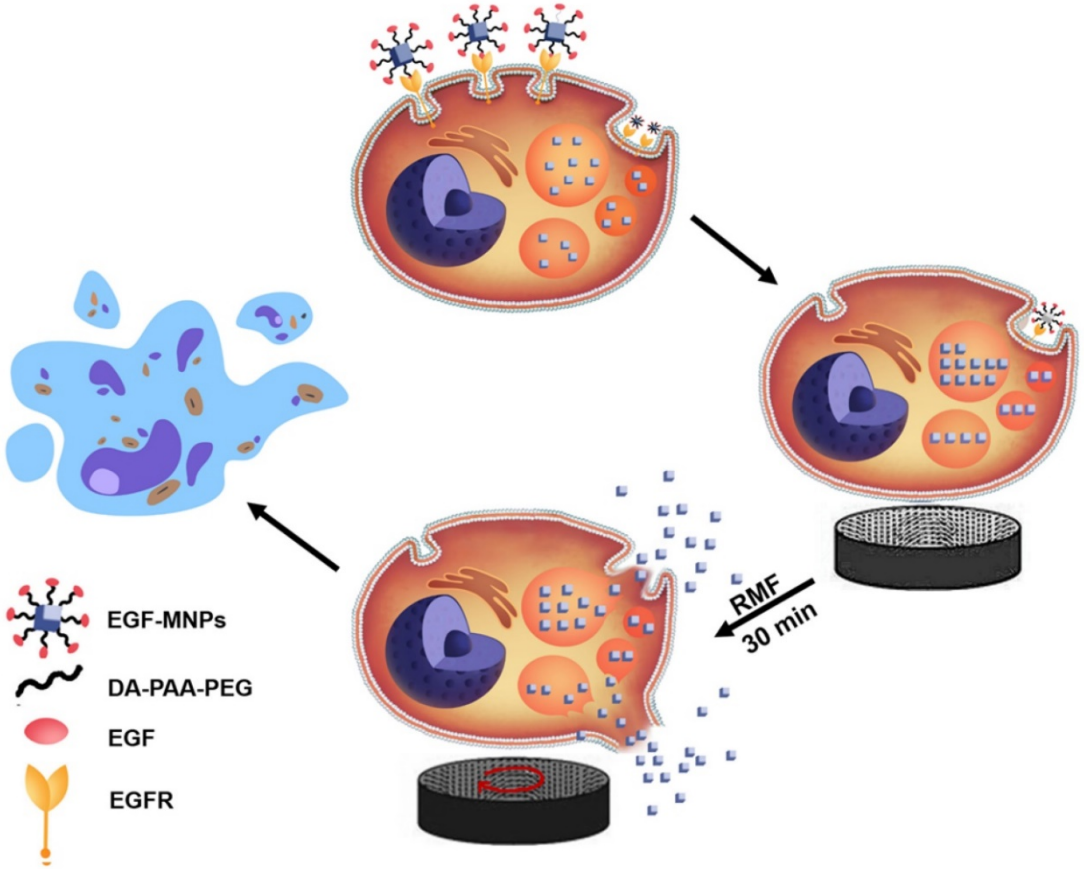

Figure 7. Scheme of the proposed mechanism of lysosome and cell membrane destruction under the RMF and cell apoptosis. EGF-functionalized MNPs link to EGFR membrane receptor and then are internalized in cancer cells, mainly accumulating in lysosomes. By applying the RMF, the MNPs form elongated aggregates which may produce the torque, and associated forces, required for mechanically disrupting lysosomal membranes and also the plasma membrane. The permeabilization of the membranes leads to direct cell destruction or apoptosis.

Conclusion

In summary, we have shown that by using a low frequency RMF the MNPs can assemble into elongated aggregates to destruct glioma cells. These aggregated MNPs can achieve the size to generate torques and produce elevated forces with relatively low magnetic field for mechanical disruption of lysosomal membranes and even the plasma membrane. The physical disruption can inhibit cancer cell growth by inducing programmed cell death and necrosis. This remote magneto-mechanical actuation approach is attractive with unique advantages without heating of neighboring tissues. Furthermore, the low frequency RMF can penetrate into human body without side effects and could considerably reduce the costs for instrumentation. Therefore, the present work offers a promising strategy for magnetic nanomedicines to noninvasively treat cancers, in particular, brain cancer.

Supplementary Material

Additional File 1:
Supplementary figures.
http://www.thno.org/v07p1735s1.pdf
Additional File 2:
Video S1. http://www.thno.org/v07p1735s2.mp4

Acknowledgements

This work was financed by National Science Foundation of China (No.81571803) and NIH (R35CA197725, R01NS077388). Y.C. thanks the Thousand Talents Plan, Shanghai Pujiang Program (No.15PJ1407800), Shanghai Science and International Cooperation Program (No. 16410724300) and Collaborative Innovation Center of Modern Bio-Manufacture Anhui University (CIMBM, BM2015005) for support. TQPU and GRP received a team grant from the Program of High-end Foreign Experts of the State Administration of Foreign Experts Affairs, China. We thank Yimei Chen at the Electron Microscopy Core Facility of University of Chicago for the assistance in TEM image analysis.

Author contributions

YC and GP designed the project and contributed magnetic-field analysis. YS and CW implemented the experiments and analyzed the data. TU, LB and ML contributed the experimental design. All the authors contributed to the manuscript writing and editing

Competing Interests

The authors have declared that no competing interest exists.

References

1. Muthana M, Kennerley AJ, Hughes R, et al. Directing cell therapy to anatomic target sites in vivo with magnetic resonance targeting. Nat Commun. 2015; 6:8009.
2. Cheng KK, Chan PS, Fan S, et al. Curcumin-conjugated magnetic nanoparticles for detecting amyloid plaques in Alzheimer's disease mice using magnetic resonance imaging (MRI). Biomaterials. 2015; 44:155-72.
3. Mura S, Nicolas J, Couvreur P. Stimuli-responsive nanocarriers for drug delivery. Nat Mater. 2013; 12:991-1003.
4. Wang R, Hu Y, Zhao N, Xu F J. Well-defined peapod-like magnetic nanoparticles and their controlled modification for effective imaging guided gene therapy. ACS Appl Mater Interfaces. 2016; 8: 11298-308.
5. Qiao R, Jia Q, Hüwel S, et al. Receptor-mediated delivery of magnetic nanoparticles across the blood–brain barrier. ACS Nano. 2012; 6:3304-10.
6. Dilnawaz F, Singh A, Mewar S, et al. The transport of non-surfactant based paclitaxel loaded magnetic nanoparticles across the blood brain barrier in a rat model. Biomaterials. 2012; 33:2936-51.
7. Marie H, Lemaire L, Franconi F, et al. Superparamagnetic Liposomes for MRI monitoring and external magnetic field−induced selective targeting of malignant brain tumors. Adv Funct Mat. 2015; 25:1258-69.
8. Cole AJ, David AE, Wang J, et al. Magnetic brain tumor targeting and biodistribution of long-circulating PEG-modified, cross-linked starch-coated iron oxide nanoparticles. Biomaterials. 2011; 32: 6291-301.
9. Kong SD, Lee J, Ramachandran S, et al. Magnetic targeting of nanoparticles across the intact blood–brain barrier. J Control Release. 2012; 164: 49-57.
10. Fan CH, Ting CY, Lin HJ, et al. SPIO-conjugated, doxorubicin-loaded microbubbles for concurrent MRI and focused-ultrasound enhanced brain-tumor drug delivery. Biomaterials. 2013; 34:3706-15.
11. Espinosa A, Di Corato R, Kolosnjaj-Tabi J, et al. Duality of iron oxide nanoparticles in cancer therapy: amplification of heating efficiency by magnetic hyperthermia and photothermal bimodal treatment. ACS Nano. 2016; 10:2436-46.
12. Ito A, Shinkai M, Honda H, et al. Heat-inducible TNF-a gene therapy combined with hyperthermia using magnetic nanoparticles as a novel tumor-targeted therapy. Cancer Gene Ther. 2001; 8: 649-54.
13. Glöckl G, Hergt R, Zeisberger M, et al. The effect of field parameters, nanoparticle properties and immobilization on the specific heating power in magnetic particle hyperthermia. J Phys Condens Matter. 2006; 18: S2935-S2949.
14. Toraya-Brown S, Seiko S, Mee R, et al. Phagocytes mediate targeting of iron oxide nanoparticles to tumors for cancer therapy. Integr Biol (Camb). 2013; 5:159-71.
15. Chiu−Lam A, Rinaldi C. Nanoscale thermal phenomena in the vicinity of magnetic nanoparticles in alternating magnetic fields. Adv Funct Mater. 2016; 22:3933-42.
16. Jordan A, Maier-Hauff K. Magnetic nanoparticles for intracranial thermotherapy. J Nanosci Nanotechnol. 2007; 7:4604-6.
17. van Landeghem FKH, Maier-Hauff K, Jordan A, et al. Post-mortem studies in glioblastoma patients treated with thermotherapy using magnetic nanoparticles. Biomaterials. 2009; 30:52-7.
18. Zhang ZQ, Song SC, et al. Thermosensitive/superparamagnetic iron oxide nanoparticle-loaded nanocapsule hydrogels for multiple cancer hyperthermia. Biomaterials. 2016; 106:13-23.
19. Ivkov R, DeNardo SJ, Daum W, et al. Application of high amplitude alternating magnetic fields for heat induction of nanoparticles localized in cancer. Clin Cancer Res. 2005; 11:7093s-7103s.
20. Thomas CR, Ferris DP, Lee JH, et al. Noninvasive remote-controlled release of drug molecules in vitro using magnetic actuation of mechanized nanoparticles. J Am Chem Soc. 2010; 132:10623-10625.
21. Golovin YI, Gribanovsky SL, Golovin DY, et al. Towards nanomedicines of the future: Remote magneto-mechanical actuation of nanomedicines by alternating magnetic fields. J Control Release. 2015; 219:43-60.
22. Master AM, Williams PN, Pothayee N, et al. Remote actuation of magnetic nanoparticles for cancer cell selective treatment through cytoskeletal disruption. Sci Rep. 2016; 6:33560-33573.
23. Cheng Y, Muroski ME, Petit DC, et al. Rotating magnetic field induced oscillation of magnetic particles for in vivo mechanical destruction of malignant glioma. J Control Release. 2016; 223:75-84.
24. Liu D, Wang L, Wang Z, et al. Magnetoporation and magnetolysis of cancer cells via carbon nanotubes induced by rotating magnetic fields. Nano Lett. 2012; 12:5117-5121.
25. Kim DH, Rozhkova EA, Ulasov IV, et al. Biofunctionalized magnetic-vortex microdiscs for targeted cancer-cell destruction. Nat Mater. 2010; 9:165-171.
26. Hapuarachchige S, Kato Y, Ngen EJ, et al. Non-temperature induced effects of magnetized iron oxide nanoparticles in alternating magnetic field in cancer cells. PloS One. 2016; 11: e0156294.
27. Zhang E, Kircher MF, Koch M, et al. Dynamic magnetic fields remote-control apoptosis via nanoparticle rotation. ACS Nano. 2014; 8:3192-3201.
28. Jacintho GVM, Brolo AG, Corio P, et al. Structural investigation of MFe_2O_4 (M= Fe, Co) magnetic fluids. J Phys Chem C. 2009;113:7684-7691.
29. Noh SH, Na W, Jang JT, et al. Nanoscale magnetism control via surface and exchange anisotropy for optimized ferrimagnetic hysteresis. Nano Lett. 2012; 12:3716-3721.

30. Chinnasamy CN, Narayanasamy A, Ponpandian N, et al. Magnetic properties of nanostructured ferrimagnetic zinc ferrite. J Phys Condens Matter. 2000; 12:7795-7805.
31. Cho MH, Lee EJ, Son M, et al. A magnetic switch for the control of cell death signaling in in vitro and in vivo systems. Nat Mater. 2012; 11:1038-1043.
32. Chung TH, Hsiao JK, Yao M, et al. Ferucarbotran, a carboxydextran-coated superparamagnetic iron oxide nanoparticle, induces endosomal recycling, contributing to cellular and exosomal EGFR overexpression for cancer therapy. RSC Adv. 2015; 5:89932-89939.
33. Mellinghoff IK, Wang MY, Vivanco I, et al. Molecular determinants of the response of glioblastomas to EGFR kinase inhibitors. N Engl J Med. 2005; 353:2012-2024.
34. Friedman HS, Bigner DD. Glioblastoma multiforme and the epidermal growth factor receptor. N Engl J Med. 2005; 353:1997-1999.
35. Master AM, Sen Gupta A. EGF receptor-targeted nanocarriers for enhanced cancer treatment. Nanomedicine. 2012; 7:1895-1906.
36. Erdal H, Berndtsson M, Castro J, et al. Induction of lysosomal membrane permeabilization by compounds that activate p53-independent apoptosis. Proc Natl Acad Sci U S A. 2005; 102:192-197.
37. Domenech M, Marrero-Berrios I, Torres-Lugo M, et al. Lysosomal membrane permeabilization by targeted magnetic nanorticles in alternating magnetic fields. ACS Nano. 2013; 7:5091-5101.
38. Serrano-Puebla A, Boya P. Lysosomal membrane permeabilization in cell death: new evidence and implications for health and disease. Ann N Y Acad Sci. 2016; 1371:30-44.
39. Contreras MF, Sougrat R, Zaher A, et al. Non-chemotoxic induction of cancer cell death using magnetic nanowires. Int J Nanomedicine. 2015; 10:2141-2153.
40. Akram F, Akram S, Wali N. Safety concerns related to ultra high field magnetic resonance imaging. Pak J Radiol. 2017; 27:38-43.
41. Allen M, Bjerke M, Edlund H, et al. Origin of the U87MG glioma cell line: Good news and bad news. Sci Transl Med. 2016; 8:354re3.
42. Dolgin E. Venerable brain-cancer cell line faces identity crisis. Nature. 2016; 537:149-150.
43. Li Z, Wang C, Cheng L, et al. PEG-functionalized iron oxide nanoclusters loaded with chlorin e6 for targeted, NIR light induced, photodynamic therapy. Biomaterials. 2013; 34:9160-9170.
44. Aits S, Kricker J, Liu B, et al. Sensitive detection of lysosomal membrane permeabilization by lysosomal galectin puncta assay. Autophagy. 2015; 11:1408-1424.
45. Lee JH, Kim JW, Levy M, et al. Magnetic nanoparticles for ultrafast mechanical control of inner ear hair cells. ACS Nano. 2014; 8:6590-6598.
46. Liu X, Liu J, Zhang S, et al. Structural, magnetic, and thermodynamic evolutions of Zn-doped Fe_3O_4 nanoparticles synthesized using a one-step solvothermal method. J Phys Chem C. 2016; 120:1328-1341.
47. Saville SL, Qi B, Baker J, et al. The formation of linear aggregates in magnetic hyperthermia: Implications on specific absorption rate and magnetic anisotropy. J Colloid Interface Sci. 2014; 424:141-151.
48. Carrey J, Hallali N. Torque undergone by assemblies of single-domain magnetic nanoparticles submitted to a rotating magnetic field. Phys Rev B. 2016; 94:184420.
49. Fung AO, Kapadia V, Pierstorff E, et al. Induction of cell death by magnetic actuation of nickel nanowires internalized by fibroblasts. J Phys Chem C. 2008; 112:15085-15088.
50. Afrin R, Yamada T, Ikai A. Analysis of force curves obtained on the live cell membrane using chemically modified AFM probes. Ultramicroscopy. 2004; 100:187-195.
51. Mamot, C. Drummond DC, Greiser U, et al. Epidermal growth factor receptor (EGFR)-targeted immunoliposomes mediate specific and efficient drug delivery to EGFR-and EGFRvIII-overexpressing tumor cells. Cancer Res. 2003; 63:3154-3161.
52. Saftig P, Klumperman J. Lysosome biogenesis and lysosomal membrane proteins: trafficking meets function. Nat Rev Mol Cell Biol. 2009; 10:623-635.
53. Boya P, Kroemer G. Lysosomal membrane permeabilization in cell death. Oncogene. 2008; 27: 6434-6451.
54. Kroemer G, Jäättelä M. Lysosomes and autophagy in cell death control. Nat Rev Cancer. 2005; 5:886-897.
55. Paz I, Sachse M, Dupont N, et al. Galectin-3, a marker for vacuole lysis by invasive pathogens. Cell Microbiol. 2010; 12:530-544.
56. Appelqvist H, Wäster P, Kågedal K, et al. The lysosome: from waste bag to potential therapeutic target. J Mol Cell Biol. 2013; 5:214-226.
57. Xu C, Yuan Z, Kohler N, et al. FePt nanoparticles as an Fe reservoir for controlled Fe release and tumor inhibition. J Am Chem Soc. 2009; 131:15346-15351.
58. Liu G, Gao J, Ai H, et al. Applications and potential toxicity of magnetic iron oxide nanoparticles. Small 2013; 9:1533-1545.
59. Li W, Yuan X, Nordgren G, et al. Induction of cell death by the lysosomotropic detergent MSDH. FEBS Lett. 2000; 470:35-39.